



## OPEN ACCESS

## EDITED BY

Belkis Sulbaran-Rangel,  
University of Guadalajara, Mexico

## REVIEWED BY

Changyin Zhu,  
Nanjing University, China  
Jiafeng Ding,  
Hangzhou Normal University, China

## \*CORRESPONDENCE

Mingzhi Huang,  
✉ mingzhi.huang@m.scnu.edu.cn

<sup>†</sup>These authors have contributed equally to this work and share first authorship

## SPECIALTY SECTION

This article was submitted to Water and Wastewater Management, a section of the journal Frontiers in Environmental Science

RECEIVED 30 November 2022

ACCEPTED 07 March 2023

PUBLISHED 20 March 2023

## CITATION

He Y, Wang X, Ke Y, Qiu Y, Zhou Q, Shen Z, Xie H, Li Y and Huang M (2023), Activation of peroxymonosulfate by cow manure biochar@1T-MoS<sub>2</sub> for enhancing degradation of dimethyl phthalate: Performance and mechanism. *Front. Environ. Sci.* 11:1112801. doi: 10.3389/fenvs.2023.1112801

## COPYRIGHT

© 2023 He, Wang, Ke, Qiu, Zhou, Shen, Xie, Li and Huang. This is an open-access article distributed under the terms of the [Creative Commons Attribution License \(CC BY\)](https://creativecommons.org/licenses/by/4.0/). The use, distribution or reproduction in other forums is permitted, provided the original author(s) and the copyright owner(s) are credited and that the original publication in this journal is cited, in accordance with accepted academic practice. No use, distribution or reproduction is permitted which does not comply with these terms.

# Activation of peroxymonosulfate by cow manure biochar@1T-MoS<sub>2</sub> for enhancing degradation of dimethyl phthalate: Performance and mechanism

Yutian He<sup>1,2†</sup>, Xinzhi Wang<sup>1†</sup>, Yuhan Ke<sup>3†</sup>, Yiquan Qiu<sup>1</sup>, Qiao Zhou<sup>1</sup>, Zheyu Shen<sup>1</sup>, Han Xie<sup>1</sup>, Yingqiang Li<sup>1</sup> and Mingzhi Huang<sup>1,4,5,6\*</sup>

<sup>1</sup>SCNU Environmental Research Institute, Guangdong Provincial Key Laboratory of Chemical Pollution and Environmental Safety & MOE Key Laboratory of Theoretical Chemistry of Environment, School of Environment, South China Normal University, Guangzhou, China, <sup>2</sup>BASIS International School, Guangzhou, China, <sup>3</sup>School of Civil Engineering and Architecture, Guangxi University, Nanning, China, <sup>4</sup>School of Resources and Environmental Sciences, Quanzhou Normal University, Quanzhou, China, <sup>5</sup>SCNU Qingyuan Institute of Science and Technology Innovation Co., Ltd, Qingyuan, China, <sup>6</sup>South China Intelligence Environment Technology (Qingyuan) Co., Ltd, Qingyuan, China

**Introduction:** Dimethyl phthalate (DMP) which has been widely detected in water is neurotoxic to humans and should be effectively eliminated. Persulfate-based advanced oxidation processes are considered to be reliable methods aiming at emerging contaminants degradation, while an efficient catalyst is urgently needed for the activation of the reaction. As a typical 2D material, 1T-MoS<sub>2</sub> is expected to be applied to the activation of persulfate owing to its abundant active sites and excellent electrical conductivity. In practical applications, 1T-MoS<sub>2</sub> has the phenomenon of reunion which affects the exposure of its catalytic sites.

**Methods:** Therefore, in this study, we used waste cow manure as a raw material to prepare biochar and achieved high exposure of 1T-MoS<sub>2</sub> activation sites by loading 1T-MoS<sub>2</sub> onto the surface of cow manure biochar through hydrothermal synthesis. The prepared composite catalytic material CMB@1T-MoS<sub>2</sub> was used to activate PMS for the degradation of DMP.

**Results:** It was found that CMB@1T-MoS<sub>2</sub> has better effect than CMB or 1T-MoS<sub>2</sub> alone for the degradation of DMP, reaching 77.65% at pH = 3. Under alkaline conditions, the degradation rate of DMP was reduced due to the inhibition of the catalytic process. Among the different coexisting anions, HCO<sub>3</sub><sup>-</sup> interfered and inhibited the degradation process the most, leading to the lowest degradation rate of DMP with 42.45%.

**Discussion:** The quenching experiments and EPR analysis showed that SO<sub>4</sub><sup>•-</sup> and •OH were the main ROS in the CMB@1T-MoS<sub>2</sub>/PMS process. This study promotes the resourceful use of cow manure and is expected to provide a novel persulfate-based advanced oxidation process catalyzed by CMB@1T-MoS<sub>2</sub> for the elimination of DMP in an aqueous environment.

## KEYWORDS

dimethyl phthalate, CMB@1T-MoS<sub>2</sub>, peroxymonosulfate, advanced oxidation processes, degradation

## 1 Introduction

Phthalic acid esters (PAEs), due to its low production cost and lack of cheaper alternative, is commonly used as plasticizer for various daily products across commerce, industry, and medical fields (Das et al., 2021; Tuan Tran et al., 2022). The production and usage of PAEs increased from 2.7 to approximately six million tons per year from 2007 to 2017 (Gao et al., 2018). Notably, due to the prevalence of the global pandemic COVID-19, it is estimated that 40,000–230,000 tons of microplastics will enter the ocean by 2040 if mask consumption continued, and dimethyl phthalate (DMP) releases into marine environment increased in a time dependent manner (De-la-Torre et al., 2022; Chen et al., 2023a). Consequently, the wide application led to exposures to the surrounding environment. PAEs have been found in soil, air, and water resources, through discharge or leaching, thus exposing them to animals, plants, and human (Liu et al., 2019a; Tuan Tran et al., 2022). United States Environmental Protection Agency, European Nation, China, and other nations have listed dimethyl phthalate along with other five PAEs as priority pollutants (Kashyap and Agarwal, 2018). Known for its neurotoxic, reproductive, and endocrine disruptive responses, DMP has adverse effects in the health of animals and plants, leading to disfunctions in red blood cells' oxygen carrying capability, induction of blood immunotoxicity, and inhibition of growth of plants (Chi et al., 2021; Chi et al., 2022; Pietrini et al., 2022). Therefore, a more efficient degradation method for the degradation of DMP is needed.

Various physical, biological, and chemical treatments have been utilized by researcher for the removal of DMP. Adsorption (Jedynak et al., 2017), atmospheric plasma (Ulucan-Altuntas et al., 2022), and biological treatments (Zhang et al., 2016; Zhou et al., 2022; Zhao et al., 2023) are mature methods removing DMP from the surrounding environment, but failing to degrade the target organic pollutant and varying performances influenced by multiple factors. Advanced oxidation processes (AOPs) have raised much attention from researcher. The generation of oxygen species in AOPs enables reliable and efficient complete degradation of targeted contaminants. The following AOPs were used in degradation of DMP: Photocatalytic oxidation (Souza et al., 2014a; Zhou et al., 2022; Zhang et al., 2023), Fenton oxidation (Pan et al., 2021; Chen et al., 2023b), persulfate oxidation (Zhou et al., 2019; Lai et al., 2021; Yang et al., 2021), electrochemical oxidation (Souza et al., 2014a; Souza et al., 2014b), ozone oxidation (Wang et al., 2009; Liu et al., 2019b), etc. Persulfate-based oxidation generates high oxidative potential sulfate radicals (2.5–3.1 V) compared with hydroxyl radicals (2.7 V) (Duan et al., 2016), exhibiting better performances for the degradation of organic pollutants. The high input of energy and additives, the potential residue of metals (i.e., irons), and relatively high operation cost of the above AOPs is outcompeted by persulfate oxidation. Researchers have successfully activated persulfate for the degradation of DMP using nZVT (nanoscale zero valent tungsten) (Zhou et al., 2019), FCBCs (iron–cerium bimetallic catalysts) (Dong et al., 2019), Fe-MOF-74 (Fe-based metal-organic framework) (Ding et al., 2021a; Ding et al., 2021b), and g-C<sub>3</sub>N<sub>4</sub> (metal-free graphitic carbon nitride) excited under visible light (Xu et al., 2020). However, those approaches include drawbacks such as high dosage of persulfate and residue sulfate,

hindering their sustainability and application in real world (Han et al., 2022). Therefore, the application of persulfate oxidation requires improved external conditions, enhancing the formation of sulfate radicals.

As heterogeneous catalysts for activation of persulfate oxidation, nanomorphous two-dimensional transition metal dichalcogenides (2D-TMDs) draw researchers' interest. One 2D-TMD, molybdenum sulfide (MoS<sub>2</sub>)'s outstanding physiochemical properties with its distinctive structure and highly reactive received a lot of attention. Researchers have utilized MoS<sub>2</sub> as catalyst activating peroxymonosulfate (PMS) in degradation of carbamazepine (Zhou et al., 2020) and tetracycline (Li et al., 2022), degradation of antibiotics wastewater (Zhu et al., 2020), and remediation of aromatic organic pollutants (Du et al., 2020), etc. Among the common crystal structures of MoS<sub>2</sub>, hexagonal MoS<sub>2</sub> stable semiconducting 2H-phase is more abundant in nature compared with the trigonal sub-stable metallic 1T-phase MoS<sub>2</sub>. 1T-MoS<sub>2</sub> have been found having better catalytic ability for the activation of PMS, due to its hydrophilic nature and metal-like conductivity (Chen et al., 2020; Wang et al., 2023). However, the clustering of flower like 1T-MoS<sub>2</sub> nanosheets compromises its catalytic capability, as less active sites are exposed.

Biochar is widely used in wastewater treatment due to its low cost, wide source and good adsorption properties (Pan et al., 2021; Chen et al., 2022). Previous studies have shown that biochar is effective in the removal of organic contaminants such as tetracycline and carbamazepine, (Guo et al., 2021; Lei et al., 2022; Su et al., 2022; Zhu et al., 2022), and has demonstrated good reusability and stability (Gan et al., 2019). In this study, we used cow dung as a raw material for biochar to prepare the catalyst CMB@1T-MoS<sub>2</sub> for AOPs by high temperature calcination and hydrothermal technique. The objectives of this study were 1) to clarify the effectiveness of CMB@1T-MoS<sub>2</sub> in activating PMS compared to CMB and 1T-MoS<sub>2</sub> alone; 2) to compare and analyze the effects of CMB@1T-MoS<sub>2</sub> dosage, PMS dosage and initial pH on the degradation of DMP in the CMB@1T-MoS<sub>2</sub>/PMS process; 3) identification of the main ROS in the CMB@1T-MoS<sub>2</sub>/PMS process. The results of this study can provide new pathways for resource utilization of cow manure and treatment of emerging contaminants.

## 2 Materials and methods

### 2.1 Materials

Cow manure used in this study to produce cow manure-derived biochar (CMB) was collected from a farm near Nanping, Fujian Province, China. Chemicals such as ammonium molybdate tetrahydrate [(NH<sub>4</sub>)<sub>6</sub>Mo<sub>7</sub>O<sub>24</sub>·4H<sub>2</sub>O, 99%], thiourea (CH<sub>4</sub>N<sub>2</sub>S, 99%), peroxymonosulfate (PMS, KHSO<sub>5</sub>), and L-histidine (C<sub>6</sub>H<sub>9</sub>N<sub>3</sub>O<sub>2</sub>, 99%) were purchased from Shanghai Macklin Biochemical Co., Ltd, China. Methanol (CH<sub>4</sub>O, ≤100%), acetonitrile (C<sub>2</sub>H<sub>3</sub>N, ≤100%), ethanol (C<sub>2</sub>H<sub>6</sub>O, ≤100%), polypropylene centrifuge tubes (15 mL, 50 mL) and standard substance (bisphenol A (BPA), ciprofloxacin (CIP), thiacloprid

(THA)) of instrumental analysis were purchased from ANPEL Laboratory Technologies (Shanghai, China) Inc. Syringe filter for sample separation and purification using syringe filter were purchased from SORFA Life Science Research Co., Ltd (Beijing, China), the target containment in this study, and p-Benzoquinone (C<sub>6</sub>H<sub>4</sub>O<sub>2</sub>, 99%) were ordered from Aladdin Chemical Co., Ltd.

## 2.2 Synthesis of cow manure-derived biochar and CMB@1T-MoS<sub>2</sub>

### 2.2.1 Synthesis of cow manure-derived biochar

After collection from a farm near Nanping, Fujian Province, China, fresh cow manures were air dried, and those lump like air-dried cow manures were powdered by an electric grinder. Those air-dried cow manure particles will then be screened by a 100-mesh sieve to further refine them and placed into a ball mill to ball mill for three times at 500 r/min. Finally, powdered cow manures were pyrolyzed in a tube furnace under argon atmosphere for 2 h at 500°C using a heating rate of 10°C/min. The final product was then referred to as cow manure-derived biochar.

### 2.2.2 Synthesis of CMB@1T-MoS<sub>2</sub>

The synthesis of 1T-MoS<sub>2</sub> starts with dissolving 4 mmol of (NH<sub>4</sub>)<sub>6</sub>Mo<sub>7</sub>O<sub>24</sub>·4H<sub>2</sub>O and 56 mmol of CS(NH<sub>2</sub>)<sub>2</sub> in 140 mL of Milli-Q. 0.12 g of L-ascorbic acid (AA) and 1 g of cow manure-derived biochar (CMB) were added after 30 min of vigorous stirring. After another 30 min of stirring, the solution was transferred into a 200 mL para-polyphenol-lined autoclave and kept at 200°C for 18 h in an oven. The product was centrifuged and washed with ethanol and Milli-Q each for three times. At last, CMB@1T-MoS<sub>2</sub> was obtained after drying in vacuum. The Schematic illustration of the route for CMB@1T-MoS<sub>2</sub> synthesis is shown in [Supplementary Figure S1](#).

## 2.3 Experiment procedure

All experiments were conducted in 500 mL beakers at room temperature. The following steps are followed for most experiments in this study. 20 mL of 100 ppm DMP stock solution is mixed with 180 mL of deionized water inside the 500 mL beaker using magnetic stirring at 500 r/min. 10 mmol/L of PMS and 0.1 g of CMB/1T-MoS<sub>2</sub> was then added to initiate the degradation experiment. A control sample will be taken at 0 min before the addition of PMS and CMB/1T-MoS<sub>2</sub>, and at 1, 5, 10, 15, 30, 60, and 90 min, 1 mL of the sample was collected and mixed with 1 mL of methanol to stop the degradation process. These samples will then be diluted with 8 mL of Milli-Q and filtered through nylon filter membranes that have a pore size 0.22 μm using a syringe.

During the degradation experiment, five different conditions-a blank control group containing only of DMP, dosing CMB only, PMS only, CMB/PMS, and CMB@1T-MoS<sub>2</sub>/PMS were conducted. Furthermore, different dosage of PMS (1 mmol/L, 2 mmol/L, 5 mmol/L, and 20 mmol/L), different pH value (3, 5, 7, 9, 11), different dosage of CMB@1T-MoS<sub>2</sub> (0.05 g/L, 0.1 g/L, 0.2 g/L, 0.5 g/

L, and 1.0 g/L), and various coexisting anions (Cl<sup>-</sup>, HCO<sub>3</sub><sup>-</sup>, NO<sub>3</sub><sup>-</sup>, PO<sub>3</sub><sup>-</sup>) were carefully modified, respectively to test influence factors of this experiment. TBA, EtOH, L-histidine and p-BQ were used as quenching reagents. The degradation kinetics of this experiment was calculated to be in accordance with the pseudo-first-order kinetic equation as follows:

$$-\ln\left(\frac{C}{C_0}\right) = k_{obs}t \quad (1)$$

where C<sub>0</sub> and C represent the initial and residual concentrations of DMP, respectively; k<sub>obs</sub> (min<sup>-1</sup>) is the apparent kinetic constant.

## 2.4 Analytical techniques

Scanning electron microscope (SEM, ZEISS Gemini 300) was used to identify the surface morphology of CMB@1T-MoS<sub>2</sub>, CMB and 1T-MoS<sub>2</sub>, along with energy spectrometer (EDS, Energy Dispersive Spectrometer) used to analyze the elemental composition, content, and distribution of CMB@1T-MoS<sub>2</sub>, CMB and 1T-MoS<sub>2</sub>. X-ray photoelectron spectroscopy (XPS, Thermo Scientific K-Alpha) and X-ray diffraction (XRD, Regaku SmartLab) were used for the qualitative and quantitative analysis of the elemental composition and crystal phase composition of CMB@1T-MoS<sub>2</sub>, CMB and 1T-MoS<sub>2</sub>. Fourier Transform Infrared spectrum (FT-IR spectrum, Thermo Nicolet iN10) and Raman spectrum (WiTech alpha300R) were used to identify the molecular structural properties as well as typical characteristic functional groups of CMB@1T-MoS<sub>2</sub>, CMB and 1T-MoS<sub>2</sub>. Nitrogen adsorption and desorption experiments (Micromeritics APSP 2460) were used to determine the specific surface area, pore volume and average pore diameter of the materials. UPLC system (Agilent 1,290 Series) equipped with a triple quadrupole mass (QQQ-MS/MS, Agilent G6495 Series) was used to quantify the concentration of DMP in samples. Chromatographic separations in quantitative analysis were carried out by a Zorbax SB-C18 column (Agilent, 3.5 μm × Ø2.1 mm × 100 mm). The mobile phase was the mixture of 40% ultra-pure water containing 0.1% formic acid and 60% acetonitrile. The flow rate was 0.3 mL min<sup>-1</sup> and the column temperature was kept at 40°C. The intermediate products of DMP were detected via a UPLC system (Agilent 1,290 Series) equipped with a quadrupole time-of-flight quadrupole mass (Q-TOF-MS/MS, Agilent G6545 Series). The column type used for qualitative analysis was Eclipse Plus C18 column (Agilent, 1.8 μm × Ø3.0 mm × 150 mm). Ultra-pure water containing 0.1% formic acid and acetonitrile were used as mobile phases at a flow rate of 0.3 mL min<sup>-1</sup> with the gradient method described as follows. The initial composition was 90% Ultra-pure water containing 0.1% formic acid (mobile phase A), held for 9 min, followed by a decrease to 70% A (9–15 min). Next, the ratio of mobile phase A continuously declined to 40% (15–20 min). Then a further decrease to 10% A (20–27 min), which was maintained until the end of the analysis (27–30 min). The capillary voltage was set at 3.50 kV. The gas temperature and sheath gas temperature were set at 325°C and 350°C, respectively. The drying gas flow and sheath gas flow were set at 10 L min<sup>-1</sup> and 11 L min<sup>-1</sup>.

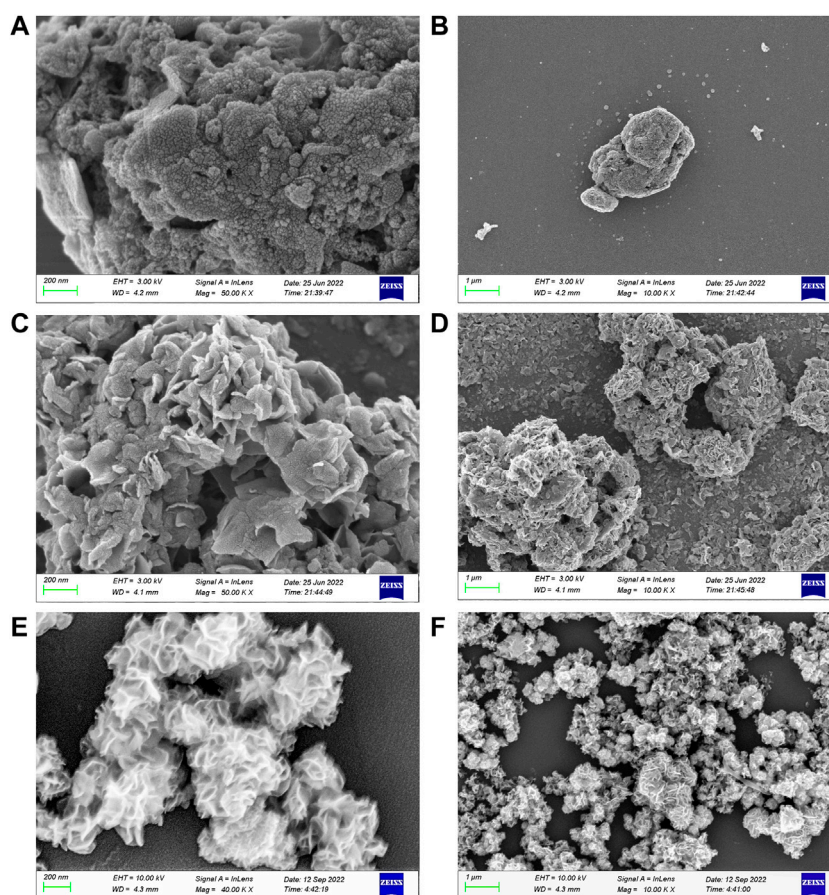


**FIGURE 1**  
(A, B) SEM images of CMB, (C, D) CMB@1T-MoS<sub>2</sub>, (E, F) 1T-MoS<sub>2</sub>.

## 3 Results and discussion

### 3.1 Characterization

The morphology, microstructure, and surface elemental composition of CMB@1T-MoS<sub>2</sub>, CMB, and 1T-MoS<sub>2</sub> were explored by SEM and EDS mapping techniques. As shown in **Figures 1A, B**, cow manure derived biochar appears to have porous and not smooth surface, providing substantial number of active sites, thus enabling MoS<sub>2</sub> to load on the surface. In contrast in **Figures 1C, D**, the SEM images of CMB@1T-MoS<sub>2</sub> shows a large number of MoS<sub>2</sub> nanosheets loaded on the surface of biochar. Furthermore, most of the MoS<sub>2</sub> nanosheets were uniformly dispersed on the biochar substrate, showing a high degree of exposure. In **Figures 1E, F**, clustered nanoflower morphology of the single MoS<sub>2</sub> could be observed. This phenomenon is attributed to the presence of van der Waals forces, electrostatic attraction and surface energy between the nanosheets, which tend to agglomerate and reach a more stable state (Liu et al., 2021; Yin et al., 2022). Further, the composition analysis of these three materials are performed by an EDS measurement. The corresponding element mapping results are presented in **Supplementary Figure S2**. It can be visually observed

that Mo and S elements are uniformly distributed on the surface of CMB@1T-MoS<sub>2</sub>, indicating the successful synthesis and loading of 1T-MoS<sub>2</sub>.

Raman spectroscopy and FT-IR spectroscopy are used to characterize the crystalline phases, characteristic defects, and characteristic functional groups of the experimental materials. In **Figure 2A**, both CMB@1T-MoS<sub>2</sub> and 1T-MoS<sub>2</sub> exhibit typical characteristic vibrational modes of molybdenum disulfide, where the peaks at wavelengths 147.8, 238.4, and 337.1 cm<sup>-1</sup> represent the J<sub>1</sub>, J<sub>2</sub> and J<sub>3</sub> characteristic vibrational modes of the 1T phase, respectively (Li et al., 2020). Meanwhile, 1T-MoS<sub>2</sub> loaded on the CMB exhibited a more responsive characteristic peak compared to 1T-MoS<sub>2</sub> alone. This is attributed to the fact that CMB acts as a substrate for hydrothermal synthesis, which facilitates the dispersion of 1T-MoS<sub>2</sub> nanosheets, resulting in a reduced degree of stacking and a more pronounced Raman activity of the corresponding vibrational moieties. Additionally, the characteristic vibrational peaks, D peak and G peak, representing C-atom lattice defects and C-atom sp<sup>2</sup> hybridization were also detected in the Raman spectrum of CMB. In **Figure 2B**, FT-IR spectra is used to identify the characteristic functional groups of the three materials. Among them, the characteristic peaks of C-C, M-O, C=O, S=S, Mo-S, C-H are present nearby the wavelengths 1,620.5, 1,400.1, 1,107.5, 1,027.0,

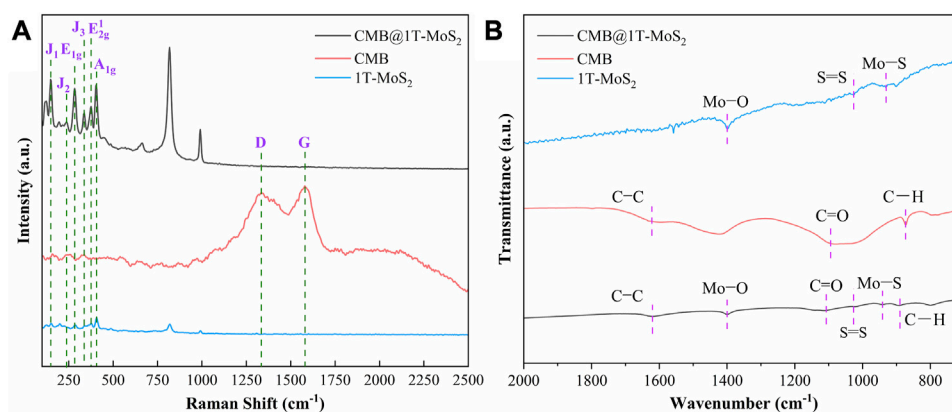


**FIGURE 2**  
(A) Raman spectra and (B) FT-IR spectra of CMB@1T-MoS<sub>2</sub>, CMB, and 1T-MoS<sub>2</sub>.

941.1, 889.5 cm<sup>-1</sup>, respectively. It is worth noting that in FT-IR analysis, the characteristic peak responses of some functional groups are relatively weak such as C-C, S=S, etc. This is mainly due to the relative structural symmetry of these groups, resulting in slight dipole changes and corresponding weak IR activity, which are difficult to be detected significantly in FT-IR spectra.

XRD and XPS were analyzed to further investigate the crystalline characteristics of the materials. In Figure 3A it can be seen that in comparison with the powder diffraction file of 2H-MoS<sub>2</sub> (PDF#37-1,492), the characteristic diffraction peaks of the characteristic crystal planes (0 0 2), (1 0 0), (1 0 1), and (1 1 0) are identified for CMB@1T-MoS<sub>2</sub> and 1T-MoS<sub>2</sub>, respectively. The (0 0 2) diffraction peaks of CMB@1T-MoS<sub>2</sub> and 1T-MoS<sub>2</sub> are brightly shifted and the diffraction peaks of CMB@1T-MoS<sub>2</sub> appear at  $2\theta = 9.1^\circ$ , which is consistent with the previously reported (0 0 2) characteristic crystal plane of 1T-MoS<sub>2</sub>. Based on the XRD results, it was found that the experimentally prepared molybdenum disulfide has a smaller characteristic derivative peak than the powdered bulk-MoS<sub>2</sub>, which leads to the conclusion that the experimentally prepared molybdenum disulfide has a larger layer spacing, while the diffraction peak position of 1T-MoS<sub>2</sub> loaded on CMB is closer to the reference value of the 1T phase, and the corresponding diffraction peak has a better response, so the presence of CMB as a substrate promotes the formation of 1T-MoS<sub>2</sub> crystals and the transformation of the crystalline phase. In addition, XPS was used to quantify the proportions of 1T phase in CMB@1T-MoS<sub>2</sub> and 1T-MoS<sub>2</sub> and to identify the characteristic binding bonds in CMB. Figures 3B–F exhibit the deconvolution of the Mo 3d, S 2p, C 1s spectrum for these materials. The peaks at approximate 228.7 eV and 231.8 eV of CMB@1T-MoS<sub>2</sub> correspond to with binding energies of Mo (IV) 3d<sub>5/2</sub> and 3d<sub>3/2</sub> in 1T phase. Similarly, the peaks at 229.4 eV and 232.8 eV of CMB@1T-MoS<sub>2</sub> are attributed to 2H phase. By calculating the peak area, the proportion of 1T phase in CMB@1T-MoS<sub>2</sub> is 78.32%, and the proportion of 1T phase in 1T-MoS<sub>2</sub> is 73.21%. In addition, the peaks at 283.1, 284.8, and 287.2 eV in the CMB represent the C-C, C-O, and -COOH, respectively. The nitrogen adsorption-desorption isotherm of CMB and CMB@1T-MoS<sub>2</sub> are shown in Figure 4. It can be seen that there is no obvious saturation adsorption plateau in both isotherms, which indicates

that the corresponding pore structures of the two materials are irregular. The BET surface areas of CMB and CMB@1T-MoS<sub>2</sub> were 6.12 m<sup>2</sup>/g and 9.97 m<sup>2</sup>/g, respectively (Supplementary Table S1). Therefore, CMB@1T-MoS<sub>2</sub> can provide more active sites to activate PMS.

## 3.2 Influence factors to DMP degradation

### 3.2.1 Effects of different reaction processes on DMP degradation

To evaluate the effect of different reaction processes on DMP elimination, six control processes were set up for degradation experiments (CMB@1T-MoS<sub>2</sub>/PMS, CMB@1T-MoS<sub>2</sub>, 1T-MoS<sub>2</sub>/PMS, CMB/PMS, PMS, Blank). Figure 5A shows that in the blank experiment, DMP was merely degraded by 5.79% within 90 min. In addition, only 12.43% and 13.12% of DMP were eliminated in the process with PMS or CMB @1T-MoS<sub>2</sub> alone. This indicates that neither the self-activation capacity of PMS nor the adsorption capacity of CMB@1T-MoS<sub>2</sub> is excellent. Furthermore, the degradation efficiencies of DMP were significantly enhanced in the CMB/PMS and 1T-MoS<sub>2</sub>/PMS processes with 32.17% and 56.10%, respectively. And when CMB@1T-MoS<sub>2</sub> was introduced to activate PMS, the DMP degradation rate reached a maximum of 77.65%. The degradation kinetic results presented in Supplementary Figure S3 show that in the CMB@1T-MoS<sub>2</sub>/PMS process, the apparent rate constant  $k_{obs}$  is 0.02042 min<sup>-1</sup>, which is much larger than the results in other reaction processes. Such a significant enhancement is attributed to the dispersive loading of 1T-MoS<sub>2</sub> on the surface of cow dung biochar, avoiding the stacking of nanosheet layers. This allowed the full exposure of a large number of 1T-MoS<sub>2</sub> activation sites. On the other hand, the Mo-O-C interfacial coupling active center will be formed between 1T-MoS<sub>2</sub> nanosheets and CMB, which effectively promotes the electron transfer in the catalytic system and achieves excellent catalytic and degradation effects (Amiin et al., 2017). In addition, the introduction of 1T-MoS<sub>2</sub> will induce electrons transfer from the adjacent carbon atoms to S atoms, thereby breaking the inertia of carbon skeleton sp<sup>2</sup> hybridization and improving the surface charge distribution of carbon atoms, which in turn leads to the

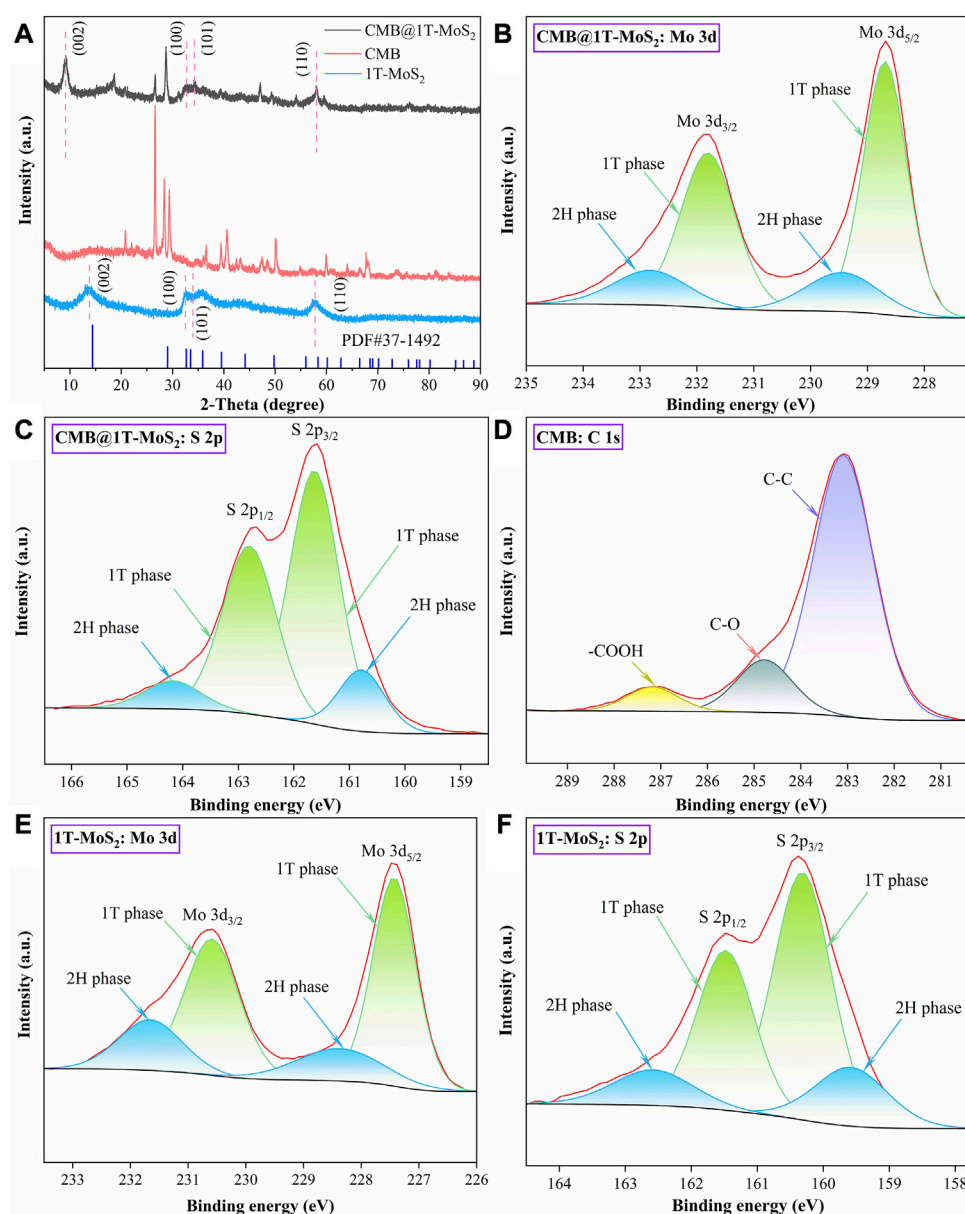


**FIGURE 3**

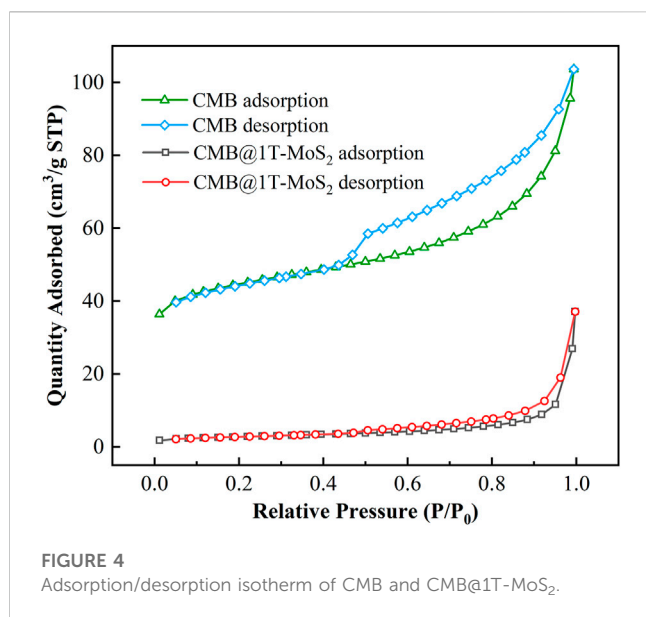
(A) XRD of CMB@1T-MoS<sub>2</sub>, CMB, and 1T-MoS<sub>2</sub>. The deconvoluted XPS results of high resolution (B, C) Mo 3d and S 2p for CMB@1T-MoS<sub>2</sub>, (D) C 1s for CMB, and (E, F) Mo 3 and S 2p for 1T-MoS<sub>2</sub>.

improvement of the electron transfer performance of CMB@1T-MoS<sub>2</sub>. Furthermore, three typical organic pollutants (bisphenol A (BPA), ciprofloxacin (CIP), thiacloprid (THA)) were selected to examine the degradation efficiency of the CMB@1T-MoS<sub>2</sub>/PMS process. The results showed that the CMB@1T-MoS<sub>2</sub>/PMS process has good generalizability for degrading organic pollutants in water (Supplementary Figure S9).

### 3.2.2 Effects of different initial pH, CMB@1T-MoS<sub>2</sub> and PMS dosage

Given that CMB@1T-MoS<sub>2</sub>/PMS has the greatest catalytic efficiency, the influence of different initial pH, CMB@1T-MoS<sub>2</sub> dosage and PMS dosage on DMP degradation was investigated

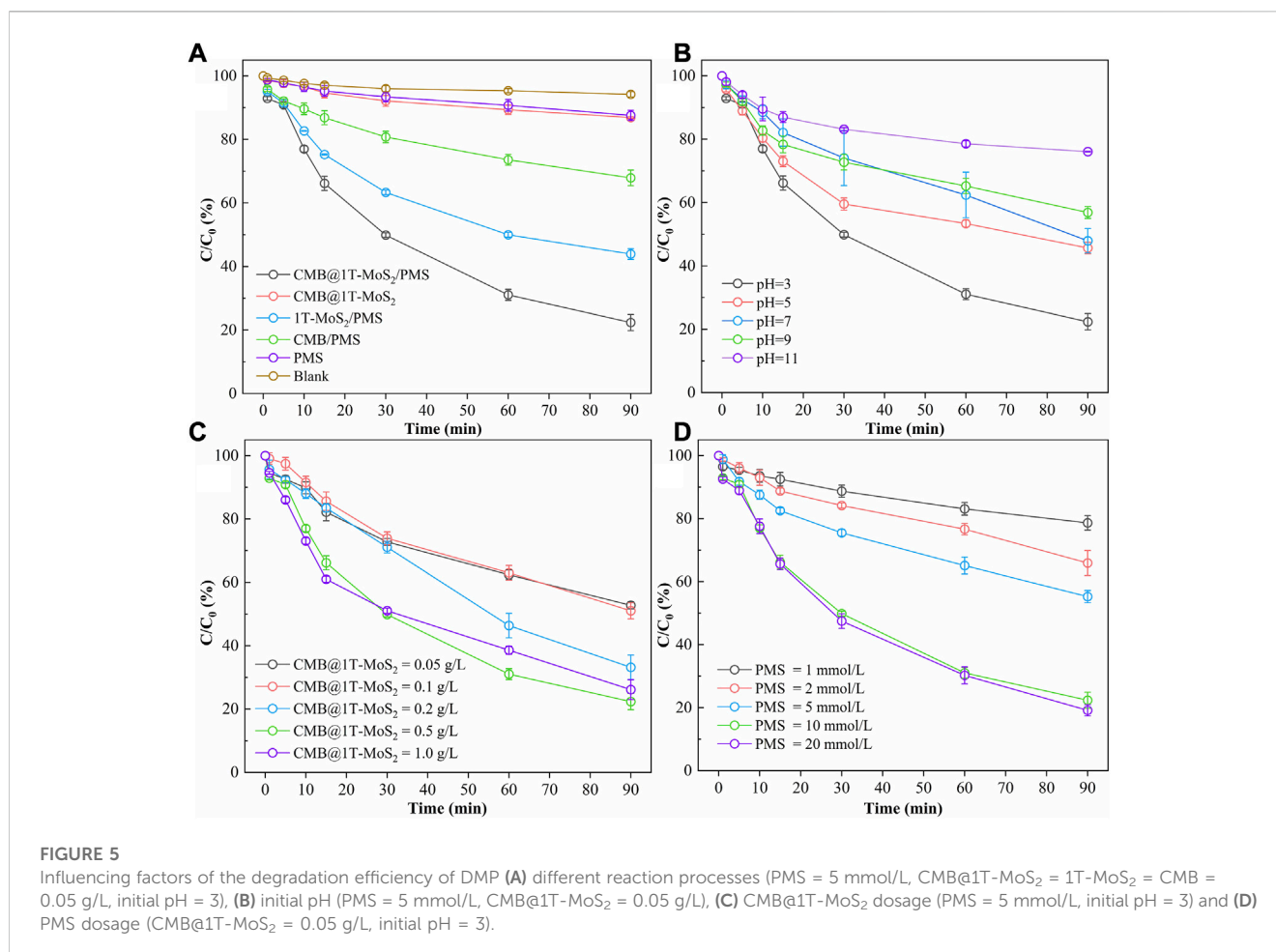
through controlled experiments. Difference in initial pH is also shown to have great impact on DMP degradation under the same condition of 10 mmol/L of PMS and 0.1 g of CMB@1T-MoS<sub>2</sub>, according to Figure 5B. The degradation ratio of DMP is 68.11% and 54.43% at pH = 3 and pH = 5, respectively compared to that of 23.93% at pH = 11. The corresponding kinetic rate constant  $K_{obs}$  was reduced from 0.00241 min<sup>-1</sup> to 0.01965 min<sup>-1</sup> (Supplementary Figure S4). This result showed that CMB@1T-MoS<sub>2</sub>/PMS has a better catalytic degradation efficiency under acidic conditions. This result is mainly attributed to the effect of pH on the catalytic process as well as on the ROS conversion process. On one hand, acidic conditions can promote the dissociation of unsaturated S atoms at the edge of 1T-MoS<sub>2</sub> to S<sup>2-</sup> and trigger a series of valence changes of

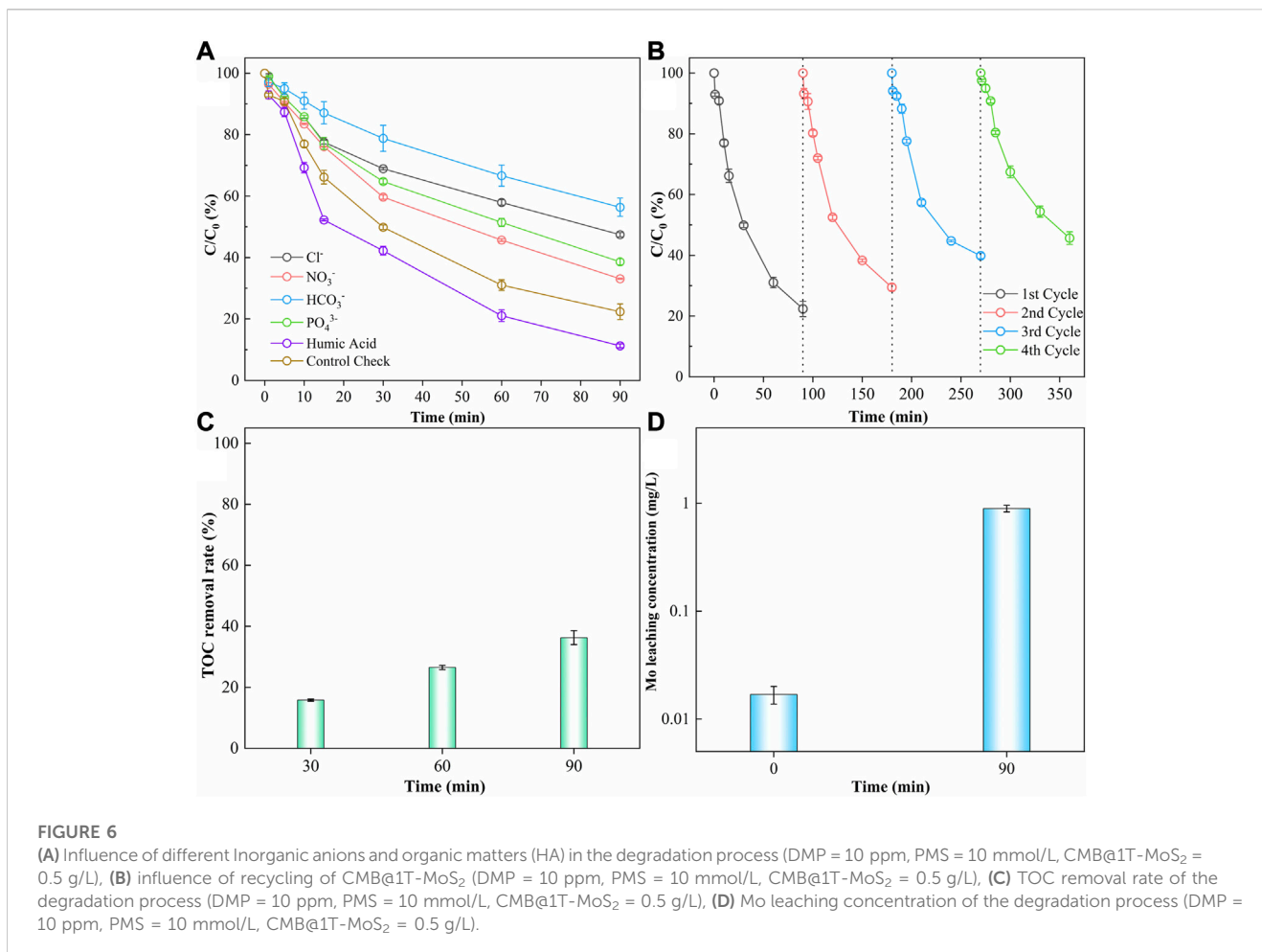


Mo by S<sup>2-</sup> trapping protons to form H<sub>2</sub>S. Meanwhile, the active unsaturated Mo 4d orbital transfers electrons to PMS, causing the peroxide bond of PMS to be broken to form SO<sub>4</sub>• and Mo(V).

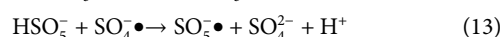
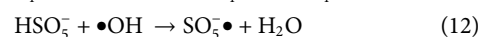
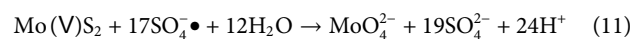
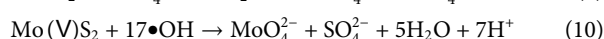
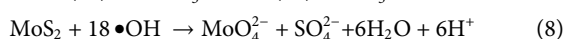
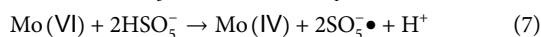
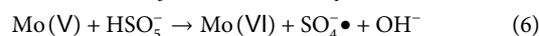
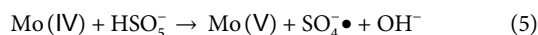
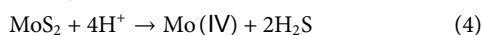
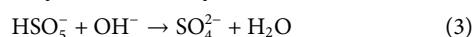
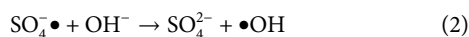
Subsequently, Mo(V) continues to transfer electrons to PMS and becomes Mo(VI). Eventually, the PMS in solution reduces the generated Mo(VI) to Mo(IV), leading to a redox process (Eqs. 2–7) (Wu et al., 2022). Hence, when the initial pH gradually increased, the activation process of 1T-MoS<sub>2</sub> on PMS was inhibited resulting in a decrease in the degradation rate of DMP. On the other hand, as the initial pH increases, a large amount of SO<sub>4</sub>• reacts with OH<sup>-</sup> to convert to SO<sub>2</sub>-4 and •OH. However, the redox potential and half-life of •OH are lower than those of SO<sub>4</sub>•, which reduces the reactivity of the oxidation process and leads to a decrease in the degradation rate of DMP.

Figures 5C, D shows that the dosage of both CMB@1T-MoS<sub>2</sub> and PMS had effects on the DMP degradation. With the increase of CMB@1T-MoS<sub>2</sub> dosage from 0.05 g/L to 1.0 g/L, the degradation rate of DMP increased from 47.24% to 73.87%. The corresponding kinetic rate constant K<sub>obs</sub> also increased from 0.00684 min<sup>-1</sup> to 0.01912 min<sup>-1</sup> (Supplementary Figure S5). It is noteworthy that with the increase of CMB@1T-MoS<sub>2</sub> dosing, the degradation rate of DMP growth trend slows down. This may be due to the insufficient amount of PMS dosing in the system. In addition, during the reaction, 1T-MoS<sub>2</sub> and its reaction intermediate Mo(V)S<sub>2</sub> consume SO<sub>4</sub>• and •OH to generate MoO<sub>2</sub>-4 (Eqs. 8–11). And since the redox potential of MoS<sub>2</sub>/MoO<sub>2</sub>-4 (~-0.43 V) is much lower than that of •OH/OH<sup>-</sup> (2.2 eV–2.8 eV) and SO<sub>4</sub>•/SO<sub>2</sub>-4 (2.5 eV–3.1 eV), it caused an inhibitory effect on the degradation of DMP.





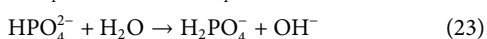
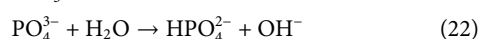
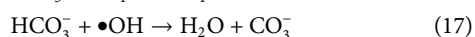
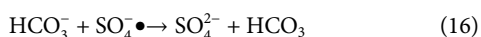
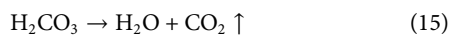
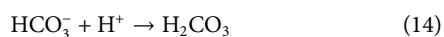
It is obvious that there is a positive correlation between the dosage of PMS and the degradation rate of DMP. As the PMS dosage increased from 1 mmol to 20 mmol/L, the degradation rate of DMP increased significantly from 21.36% to 80.85%. The corresponding kinetic rate constant  $K_{obs}$  increased from  $0.00241 \text{ min}^{-1}$  to  $0.01965 \text{ min}^{-1}$  (Supplementary Figure S6). Meanwhile, the degradation rate of DMP was 77.65% when the PMS dosage was 10 mmol/L, which was similar to the effect of PMS of 20 mmol/L. This should be on account of the fact that CMB@1T-MoS<sub>2</sub> is limited and high concentration of PMS is self-quenching to consume a certain amount of ROS in the process (Eqs. 12, 13).



### 3.2.3 Influence of different inorganic anions

Due to the potential presence of inorganic anions in the aqueous environment that could negatively impact AOPs, the investigation of the effects of coexisting anions ( $\text{Cl}^-$ ,  $\text{NO}_3^-$ ,  $\text{HCO}_3^-$ ,  $\text{PO}_4^{3-}$ , and Humic Acid) on DMP degradation by CMB@1T-MoS<sub>2</sub>/PMS process is implemented. According to Figure 6A, the degradation rate of DMP is most reduced by the presence of  $\text{HCO}_3^-$ .  $\text{HCO}_3^-$  reacts with  $\text{H}^+$  (Eqs. 14, 15), thus lowering the acidity of the solution and hindering the activation of PMS by CMB@1T-MoS<sub>2</sub>. In addition,  $\text{HCO}_3^-$  also reacts with  $\bullet\text{OH}$  and  $\text{SO}_4^{\bullet-}$ , resulting in the generation of weakly oxidized  $\text{HCO}_3^{\bullet}$  (Eqs. 16, 17), which also prevents the degradation of the system.  $\text{Cl}^-$  and  $\text{NO}_3^-$  also inhibit the degradation of DMP causing by the reaction of both with  $\bullet\text{OH}$  and  $\text{SO}_4^{\bullet-}$ , producing radicals with lower redox potentials (Eqs. 18–21). With the addition of  $\text{PO}_3\text{-4}$ , the degradation of DMP is slightly reduced, as  $\text{PO}_3\text{-4}$  underwent hydrolysis to produce  $\text{HPO}_2\text{-4}$  and  $\text{H}_2\text{PO}_4^-$  (Eqs. 22, 23) inhibiting degradation by increasing pH for the degradation system. However, studies have shown that  $\text{PO}_3\text{-4}$  and  $\text{HPO}_2\text{-4}$  can effectively break the O-O bond of PMS and promote the production of  $\text{SO}_4^{\bullet-}$  in the system,

thus enhancing the degradation process (Duan et al., 2021). The degradation rate of DMP is greatly enhanced by the presence of humic acid (HA) due to two reasons. Firstly, as a weak acid, humic acid lowered the pH of the process, promoting the catalytic efficiency of CMB@1T-MoS<sub>2</sub> on PMS, thus increasing the degradation rate. On the other hand, previous reports have shown that the abundant functional groups on the surface of HA will bind to neonicotinoids through van der Waals forces and hydrogen bonds to form new substances. This mechanism would lead to a decrease in the detectable concentration of DMP.



### 3.2.4 Reusability of CMB@1T-MoS<sub>2</sub> in DMP degradation

In order to evaluate the practical application of CMB@1T-MoS<sub>2</sub>, the reusability and stability of CMB@1T-MoS<sub>2</sub> are investigated in this paper. As shown in Figure 6B, the degradation rate of DMP decreased from 77.65% to 54.34% as CMB@1T-MoS<sub>2</sub> was reused four times. This result may be due to the fact that the residual DMP and its intermediates on the surface of CMB@1T-MoS<sub>2</sub> hinder the catalytic reaction of CMB@1T-MoS<sub>2</sub> with PMS. In addition, after many repeated uses, the own structural properties of CMB@1T-MoS<sub>2</sub> may also be the reason for the reduced degradation rate of DMP. To investigate the changes in the surface and structural states of CMB@1T-MoS<sub>2</sub>, the reused CMB@1T-MoS<sub>2</sub> was washed and freeze-dried for XPS and XRD analysis (Supplementary Figures S7, S8). Comparing the CMB@1T-MoS<sub>2</sub> before and after the reaction, it was found that the position of the characteristic peaks and the ratio of the crystalline phase composition were almost unchanged, indicating that the CMB@1T-MoS<sub>2</sub> still maintained good material properties after the reaction.

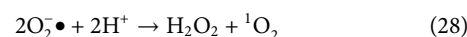
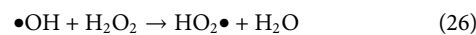
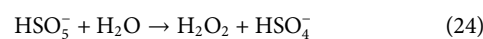
### 3.2.5 TOC removal rate and Mo ion leaching concentration

As shown in Figures 6C, D, after the reaction, the TOC removal rate of the system was 36.29% and the leaching concentration of Mo changed from the initial 0.017 ppm to 0.895 ppm the TOC removal rate was lower than the DMP degradation rate, indicating the presence of incomplete mineralized intermediates in the degradation system.

## 3.3 Identification of reactive oxygen species

Quenching experiments and EPR spectroscopy were performed in order to investigate the contribution of different

reactive oxygen species in the CMB@1T-MoS<sub>2</sub>/PMS process. In the quenching experiments, ethanol was used as a quencher for  $\bullet\text{OH}$  ( $k_{\text{OH}/\text{EtOH}} = 1.6 \times 10^7 \text{ M}^{-1} \text{ s}^{-1}$ ) and  $\text{SO}_4^{\bullet-}$  ( $k_{\text{SO}_4^{\bullet-}/\text{EtOH}} = 1.9 \times 10^9 \text{ M}^{-1} \text{ s}^{-1}$ ), and tert-butanol (TBA) was used as a quencher for  $\bullet\text{OH}$  [ $(3.8\text{--}7.6) \times 10^8 \text{ M}^{-1} \text{ s}^{-1}$ ]. The quenching effect of TBA on  $\text{SO}_4^{\bullet-}$  ( $k_{\text{SO}_4^{\bullet-}/\text{TBA}} = (4.0\text{--}9.1) \times 10^5 \text{ M}^{-1} \text{ s}^{-1}$ ) was negligible compared to  $\bullet\text{OH}$ . L-histidine was used to quench  $^1\text{O}_2$ , and p-benzoquinone (p-BQ) was used to quench  $\text{O}_2^{\bullet-}$ . In Figure 7A, the degradation rates of DMP were 10.84% and 69.68% after the addition of ethanol and tert-butanol, respectively. And after adding L-histidine and p-BQ, the degradation rates of DMP were 51.29% and 75.94%, respectively. The control experiment showed a degradation rate of 76.4%. The results of the quenching experiments showed that  $\text{SO}_4^{\bullet-}$  dominated the degradation experiments with the largest contribution to DMP in the CMB@1T-MoS<sub>2</sub>/PMS system. Secondly, the non-radical pathway dominated by  $^1\text{O}_2$  also had a significant effect on the degradation of DMP. EPR spectroscopy was performed to further confirm the generation of  $\bullet\text{OH}$ ,  $\text{SO}_4^{\bullet-}$ ,  $\text{O}_2^{\bullet-}$ , and  $^1\text{O}_2$  by using DMPO and TEMP as spin traps, respectively. In Figure 7B, EPR signals representing DMPO- $\bullet\text{OH}$  and DMPO- $\text{SO}_4^{\bullet-}$  can be detected. However, the peak intensity of  $\bullet\text{OH}$  does not show a typical ratio of 1:2:2:1 because the signal of  $\bullet\text{OH}$  is interfered by the offset of the strongly  $\text{SO}_4^{\bullet-}$  signal; Figure 7C shows a significant EPR signal with a 1:1:1 peak pattern, revealing the appearance of  $^1\text{O}_2$  in the process. Besides, the weak signal of  $\text{O}_2^{\bullet-}$  also appeared in Figure 7D. The detection of the ROS signals corroborates the results of the quenching experiments. The chemical equations for the generation of these ROS are as follows (Eqs. 24–28):



## 3.4 Degradation pathways of DMP

To further investigate the possible degradation pathways of DMP, UPLC-Q-TOF-MS/MS was used to detect the possible degradation intermediate products of DMP. According to the results of the qualitative analysis, the degradation pathway of DMP probably includes the following two ways (Figure 8). First, the benzene ring in the DMP molecule is attacked by  $\bullet\text{OH}$  and undergoes a hydrogen abstraction reaction (P1). Next, the C-O bond on the ester group is broken and the  $\bullet\text{OH}$  undergoes an electrophilic reaction at the break, which leads to the formation of carboxyl groups (P2). With further attack by reactive oxygen species, one of the carboxyl groups breaks the C-C bond with the benzene ring to form product 3 (P3). Further, the benzene ring is cleaved to form compound P4. The final contaminant is mineralized to form CO<sub>2</sub> and water. In pathway 2, at first, the ester group in the DMP molecule is attacked and the  $\bullet\text{OH}$  undergoes an electrophilic substitution

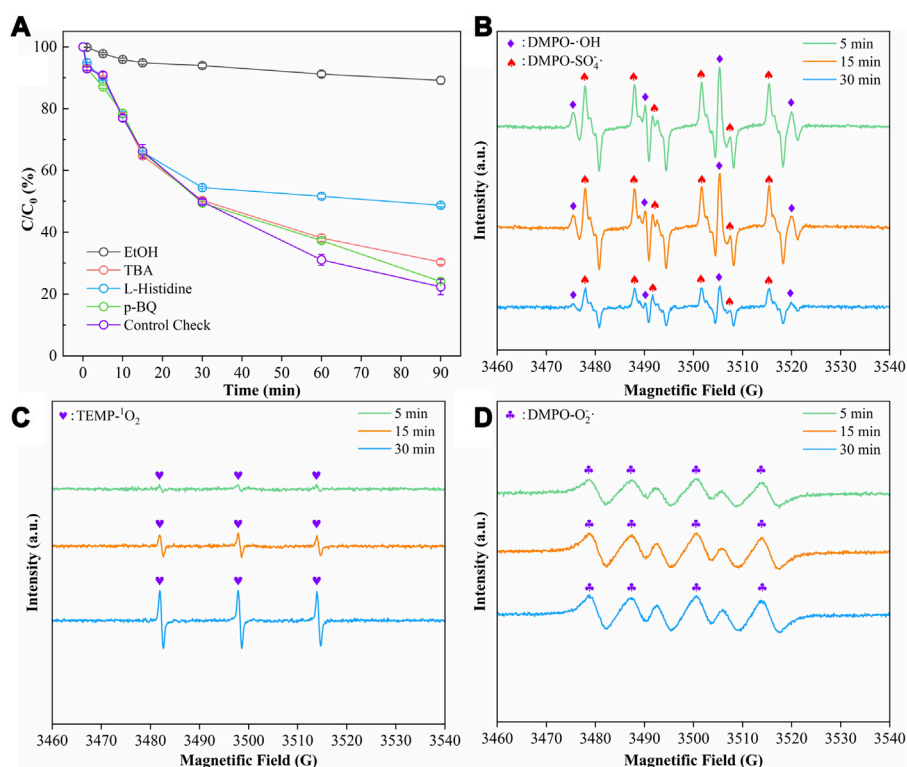


**FIGURE 7** (A) The inhibiting effects of different quenching reagents on the DMP degradation efficiency (DMP = 10 ppm, pH = 3, PMS = 10 mmol/L, EtOH = 1.2 mol/L, TBA = 1.2 mol/L, L-Histidine = 10 mmol/L, p-BQ = 10 mmol/L); and EPR spectra of (B)  $\text{SO}_4^{\bullet-}$ ,  $\bullet\text{OH}$ , (C)  $^{\bullet}\text{O}_2$ , and (D)  $\text{O}-2^{\bullet}$  (DMP = 10 ppm, pH = 3, PMS = 10 mmol/L, CMB@1T-MoS<sub>2</sub> = 0.5 g/L, DMPO = 100 mmol/L, 30  $\mu\text{L}$ , TEMP = 100 mmol/L, 50  $\mu\text{L}$ ).

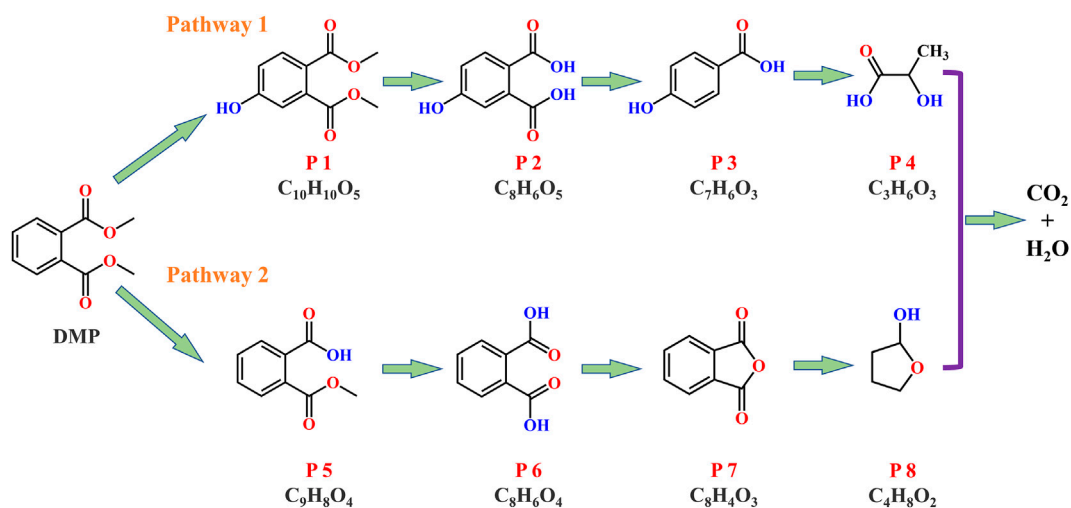


**FIGURE 8** Possible degradation pathways of DMP degradation in CMB@1T-MoS<sub>2</sub>/PMS process.

reaction to form the carboxyl group (P5), then, under the continuous attack of ROS, the carboxyl group in the molecule changes to an ether bond and finally forms with a

break between the benzene ring and the five-membered ring (P8). The mass spectra of the products are shown in [Supplementary Figures S10–S17](#).

### 3.5 Implications of this work

Firstly, CMB@1T-MoS<sub>2</sub> with higher catalytic efficiency was synthesized in this study through a series of ball milling, calcination and hydrothermal processes, which led to the effective degradation of organic pollutants in water, such as DMP. Secondly, compared with other precious metal catalysts or cobalt catalysts, the catalytic material in this experiment has a simpler preparation process and lower price, which has the prospect of large-scale production and application, and avoids the secondary pollution caused by highly toxic cobalt-containing compounds. In addition, this study provides a new way of resource utilization for the large amount of cattle manure produced by animal husbandry, and solves the problems of secondary pollution and low added value in the traditional cattle manure treatment process.

## 4 Conclusion

In this study, we propose a degradation process using CMB@1T-MoS<sub>2</sub>/PMS for the removal of DMP from water. CMB@1T-MoS<sub>2</sub> prepared by high-temperature calcination and hydrothermal method exhibited good catalytic performance for PMS and effectively degraded DMP in aqueous environment. Under alkaline conditions, the activation of PMS by Mo<sup>4+</sup> was inhibited due to the dissociation of S efficiency was reduced, thus affecting the degradation of DMP. Different anions including HCO<sub>3</sub><sup>-</sup>, Cl<sup>-</sup>, NO<sub>3</sub><sup>-</sup> and PO<sub>4</sub><sup>3-</sup> had different degrees of inhibition on the degradation process of CMB@1T-MoS<sub>2</sub>/PMS, among which HCO<sub>3</sub><sup>-</sup> had the most obvious inhibition due to the large consumption of H<sup>+</sup> and depletion of •OH and SO<sub>4</sub><sup>•-</sup>. The quenching experiments and EPR analysis showed that SO<sub>4</sub><sup>•-</sup> and <sup>1</sup>O<sub>2</sub> were the reactive oxygen species that mainly played a degradation role. In this study, CMB@1T-MoS<sub>2</sub> was prepared by using cow dung as the substrate, which not only realized the resource utilization of waste, but also effectively improved the catalytic performance of 1T-MoS<sub>2</sub> to achieve the effective degradation of organic pollutant DMP. This study be beneficial for the development of new catalysts in AOPs and the development of treatment technologies for emerging contaminants.

## Data availability statement

The raw data supporting the conclusion of this article will be made available by the authors, without undue reservation.

## Author contributions

YH: Writing-original draft, formal analysis. XW: Writing-review and editing, conceptualization, visualization. YK: Data

## References

Amiin, I. S., Pu, Z., Liu, X., Owusu, K. A., Monestel, H. G. R., Boakye, F. O., et al. (2017). Multifunctional Mo-N/C@MoS<sub>2</sub> electrocatalysts for HER. *OER, ORR, Zn-Air Batter. Adv. Funct. Mater.* 27, 1702300. doi:10.1002/adfm.201702300

curation, complete supplementary experiment, revise the review comments. YQ: Methodology. MH: Conceptualization, funding acquisition, project administration. QZ: Writing-review and editing. ZS: Software. HX: Validation. YL: Investigation. All authors contributed to manuscript revision, read, and approved the submitted version.

## Funding

This work was funded by the National Natural Science Foundation of China (41977300, 41907297), Science and Technology Program of Guangzhou (No. 202002020055), and Fujian Provincial Natural Science Foundation (No. 202011001).

## Acknowledgments

The authors appreciate Shiyanjia Lab ([www.shiyanjia.com](http://www.shiyanjia.com)) for the support of XPS and EPR test. We are also very grateful for the support of experiment from Jiahua Li from ANPEL Laboratory Technologies Inc. and Ruifang Han from SORFA Life Science Research Co., Ltd.

## Conflict of interest

Author MH was employed by SCNU Qingyuan Institute of Science and Technology Innovation Co., Ltd and South China Intelligence Environment Technology (Qingyuan) Co., Ltd.

The remaining authors declare that the research was conducted in the absence of any commercial or financial relationships that could be construed as a potential conflict of interest.

## Publisher's note

All claims expressed in this article are solely those of the authors and do not necessarily represent those of their affiliated organizations, or those of the publisher, the editors and the reviewers. Any product that may be evaluated in this article, or claim that may be made by its manufacturer, is not guaranteed or endorsed by the publisher.

## Supplementary material

The Supplementary Material for this article can be found online at: <https://www.frontiersin.org/articles/10.3389/fenvs.2023.1112801/full#supplementary-material>

Chen, J., Walker, W. R., Xu, L., Krysiak, O., She, Z., and Pope, M. A. (2020). Intrinsic capacitance of molybdenum disulfide. *ACS Nano* 14, 5636–5648. doi:10.1021/acsnano.9b10182

- Chen, Z., Wei, W., Chen, H., and Ni, B.-J. (2022). Recent advances in waste-derived functional materials for wastewater remediation. *Eco-Environment Health* 1, 86–104. doi:10.1016/j.eehl.2022.05.001
- Chen, C., Yu, G., Wang, B., Li, F., Liu, H., and Zhang, W. (2023). Lifetime prediction of non-woven face masks in ocean and contributions to microplastics and dissolved organic carbon. *J. Hazard. Mater.* 441, 129816. doi:10.1016/j.jhazmat.2022.129816
- Chen, X., Gu, X., Wang, C., Huang, L., Wu, D., Wu, H., et al. (2023). Bisulfite-assisted surface Fenton-like degradation of dimethyl phthalate by ferrihydrite-H<sub>2</sub>O<sub>2</sub> system. *Chem. Eng. J.* 452, 139309. doi:10.1016/j.ccej.2022.139309
- Chi, Z., Liu, J., Tan, S., Lin, H., Wu, W., and Li, W. (2021). Revealing the toxicity of dimethyl phthalate (DMP) to the oxygen-carrying function of red blood cells (RBCs): The iron release mechanism. *Chemosphere* 263, 128017. doi:10.1016/j.chemosphere.2020.128017
- Chi, Z., Lin, H., Wang, X., Meng, X., Zhou, J., Xiang, L., et al. (2022). Dimethyl phthalate induces blood immunotoxicity through oxidative damage and caspase-dependent apoptosis. *Sci. Total Environ.* 838, 156047. doi:10.1016/j.scitotenv.2022.156047
- Das, M. T., Kumar, S. S., Ghosh, P., Shah, G., Malyan, S. K., Bajar, S., et al. (2021). Remediation strategies for mitigation of phthalate pollution: Challenges and future perspectives. *J. Hazard. Mater.* 409, 124496. doi:10.1016/j.jhazmat.2020.124496
- De-la-Torre, G. E., Dioses-Salinas, D. C., Dobaradaran, S., Spitz, J., Nabipour, I., Keshtkar, M., et al. (2022). Release of phthalate esters (PAEs) and microplastics (MPs) from face masks and gloves during the COVID-19 pandemic. *Environ. Res.* 215, 114337. doi:10.1016/j.envres.2022.114337
- Ding, S., Wan, J., Wang, Y., Yan, Z., and Ma, Y. (2021). Activation of persulfate by molecularly imprinted Fe-MOF-74@SiO<sub>2</sub> for the targeted degradation of dimethyl phthalate: Effects of operating parameters and chlorine. *Chem. Eng. J.* 422, 130406. doi:10.1016/j.ccej.2021.130406
- Ding, S., Wan, J., Ma, Y., Wang, Y., Pu, M., Li, X., et al. (2021). Water stable SiO<sub>2</sub>-coated Fe-MOF-74 for aqueous dimethyl phthalate degradation in PS activated medium. *J. Hazard. Mater.* 411, 125194. doi:10.1016/j.jhazmat.2021.125194
- Dong, C.-D., Huang, C. P., Nguyen, T.-B., Hsiung, C.-F., Wu, C.-H., Lin, Y.-L., et al. (2019). The degradation of phthalate esters in marine sediments by persulfate over iron-cerium oxide catalyst. *Sci. Total Environ.* 696, 133973. doi:10.1016/j.scitotenv.2019.133973
- Du, M., Yi, Q., Ji, J., Zhu, Q., Duan, H., Xing, M., et al. (2020). Sustainable activation of peroxymonosulfate by the Mo(IV) in MoS<sub>2</sub> for the remediation of aromatic organic pollutants. *Chin. Chem. Lett.* 31, 2803–2808. doi:10.1016/j.ccl.2020.08.002
- Duan, X., Su, C., Zhou, L., Sun, H., Suvorova, A., Odedairo, T., et al. (2016). Surface controlled generation of reactive radicals from persulfate by carbocatalysis on nanodiamonds. *Appl. Catal. B Environ.* 194, 7–15. doi:10.1016/j.apcatb.2016.04.043
- Duan, P., Liu, X., Liu, B., Akram, M., Li, Y., Pan, J., et al. (2021). Effect of phosphate on peroxymonosulfate activation: Accelerating generation of sulfate radical and underlying mechanism. *Appl. Catal. B Environ.* 298, 120532. doi:10.1016/j.apcatb.2021.120532
- Gan, L., Zhong, Q., Geng, A., Wang, L., Song, C., Han, S., et al. (2019). Cellulose derived carbon nanofiber: A promising biochar support to enhance the catalytic performance of CoFe<sub>2</sub>O<sub>4</sub> in activating peroxymonosulfate for recycled dimethyl phthalate degradation. *Sci. Total Environ.* 694, 133705. doi:10.1016/j.scitotenv.2019.133705
- Gao, D., Li, Z., Wang, H., and Liang, H. (2018). An overview of phthalate acid ester pollution in China over the last decade: Environmental occurrence and human exposure. *Sci. Total Environ.* 645, 1400–1409. doi:10.1016/j.scitotenv.2018.07.093
- Guo, L., Zhao, J., Zhao, L., Tang, Y., Zhou, J., and Shi, B. (2021). Persulfate activation by Cr<sub>2</sub>O<sub>3</sub>/BC derived from chrome shavings for antibiotics degradation. *Chem. Eng. J.* 420, 127698. doi:10.1016/j.ccej.2020.127698
- Han, M., Wang, H., Jin, W., Chu, W., and Xu, Z. (2022). The performance and mechanism of iron-mediated chemical oxidation: Advances in hydrogen peroxide, persulfate and percarbonate oxidation. *J. Environ. Sci.* 128, 181. doi:10.1016/j.jes.2022.07.037
- Jedynak, K., Dariusz, W., and Jerzy, O. (2017). Removal of selected phthalates from aqueous solution by mesoporous-ordered carbon adsorbent. *Adsorpt. Sci. Technol.* 35, 026361741770867. doi:10.1177/0263617417708675
- Kashyap, D., and Agarwal, T. (2018). Concentration and factors affecting the distribution of phthalates in the air and dust: A global scenario. *Sci. Total Environ.* 635, 817–827. doi:10.1016/j.scitotenv.2018.04.158
- Lai, L., Ji, H., Zhang, H., Liu, R., Zhou, C., Liu, W., et al. (2021). Activation of peroxydisulfate by V-Fe concentrate ore for enhanced degradation of carbamazepine: Surface ≡V(III) and ≡V(IV) as electron donors promoted the regeneration of ≡Fe(II). *Appl. Catal. B Environ.* 282, 119559. doi:10.1016/j.apcatb.2020.119559
- Lai, Y., Guo, X., Jiang, M., Sun, W., He, H., Chen, Y., et al. (2022). Co-ZIF reinforced cow manure biochar (CMB) as an effective peroxymonosulfate activator for degradation of carbamazepine. *Appl. Catal. B Environ.* 319, 121932. doi:10.1016/j.apcatb.2022.121932
- Li, Z., Fan, R., Hu, Z., Li, W., Zhou, H., Kang, S., et al. (2020). Ethanol introduced synthesis of ultrastable 1T-MoS<sub>2</sub> for removal of Cr(VI). *J. Hazard. Mater.* 394, 122525. doi:10.1016/j.jhazmat.2020.122525
- Li, X., Guo, Y., Yan, L., Yan, T., Song, W., Feng, R., et al. (2022). Enhanced activation of peroxymonosulfate by ball-milled MoS<sub>2</sub> for degradation of tetracycline: Boosting molybdenum activity by sulfur vacancies. *Chem. Eng. J.* 429, 132234. doi:10.1016/j.ccej.2021.132234
- Liu, X., Peng, C., Shi, Y., Tan, H., Tang, S., and Chen, D. (2019). Beyond phthalate diesters: Existence of phthalate monoesters in South China house dust and implications for human exposure. *Environ. Sci. Technol.* 53, 11675–11683. doi:10.1021/acs.est.9b03817
- Liu, Y., Feng, Y., Zhang, Y., Mao, S., Wu, D., and Chu, H. (2019). Highly efficient degradation of dimethyl phthalate from Cu(II) and dimethyl phthalate wastewater by EDTA enhanced ozonation: Performance, intermediates and mechanism. *J. Hazard. Mater.* 366, 378–385. doi:10.1016/j.jhazmat.2018.12.003
- Liu, B., Han, Q., Li, L., Zheng, S., Shu, Y., Pedersen, J. A., et al. (2021). Synergistic effect of metal cations and visible light on 2D MoS<sub>2</sub> nanosheet aggregation. *Environ. Sci. Technol.* 55, 16379–16389. doi:10.1021/acs.est.1c03576
- Pan, X., Gu, Z., Chen, W., and Li, Q. (2021). Preparation of biochar and biochar composites and their application in a fenton-like process for wastewater decontamination: A review. *Sci. Total Environ.* 754, 142104. doi:10.1016/j.scitotenv.2020.142104
- Pietrini, F., Iannilli, V., Passatore, L., Carloni, S., Sciacca, G., Cerasa, M., et al. (2022). Ecotoxicological and genotoxic effects of dimethyl phthalate (DMP) on Lemna minor L. and Spirodela polyrhiza (L.) Schleid. plants under a short-term laboratory assay. *Sci. Total Environ.* 806, 150972. doi:10.1016/j.scitotenv.2021.150972
- Souza, F. L., Aquino, J. M., Miwa, D. W., Rodrigo, M. A., and Motheo, A. J. (2014). Photo-assisted electrochemical degradation of the dimethyl phthalate ester on DSA® electrode. *J. Environ. Chem. Eng.* 2, 811–818. doi:10.1016/j.jece.2014.02.003
- Souza, F. L., Aquino, J. M., Irikura, K., Miwa, D. W., Rodrigo, M. A., and Motheo, A. J. (2014). Electrochemical degradation of the dimethyl phthalate ester on a fluoride-doped Ti/β-PbO<sub>2</sub> anode. *Chemosphere* 109, 187–194. doi:10.1016/j.chemosphere.2014.02.018
- Su, X., Guo, Y., Yan, L., Wang, Q., Zhang, W., Li, X., et al. (2022). MoS<sub>2</sub> nanosheets vertically aligned on biochar as a robust peroxymonosulfate activator for removal of tetracycline. *Sep. Purif. Technol.* 282, 120118. doi:10.1016/j.seppur.2021.120118
- Tuan Tran, H., Lin, C., Bui, X.-T., Ky Nguyen, M., Dan Thanh Cao, N., Mukhtar, H., et al. (2022). Phthalates in the environment: Characteristics, fate and transport, and advanced wastewater treatment technologies. *Bioresour. Technol.* 344, 126249. doi:10.1016/j.biortech.2021.126249
- Ulucan-Altuntas, K., Saleem, M., Tomei, G., Marotta, E., and Paradisi, C. (2022). Atmospheric plasma-based approaches for the degradation of dimethyl phthalate (DMP) in water. *J. Environ. Manag.* 301, 113885. doi:10.1016/j.jenvman.2021.113885
- Wang, J., Zhou, Y., Zhu, W., and He, X. (2009). Catalytic ozonation of dimethyl phthalate and chlorination disinfection by-product precursors over Ru/AC. *J. Hazard. Mater.* 166, 502–507. doi:10.1016/j.jhazmat.2008.11.046
- Wang, X., Chen, Z., He, Y., Yi, X., Zhang, C., Zhou, Q., et al. (2023). Activation of persulfate-based advanced oxidation processes by 1T-MoS<sub>2</sub> for the degradation of imidacloprid: Performance and mechanism. *Chem. Eng. J.* 451, 138575. doi:10.1016/j.ccej.2022.138575
- Wu, L., Guo, P., Wang, X., Li, H., Li, A., and Chen, K. (2022). Mechanism study of CoS<sub>2</sub>/Fe(III)/peroxymonosulfate catalysis system: The vital role of sulfur vacancies. *Chemosphere* 288, 132646. doi:10.1016/j.chemosphere.2021.132646
- Xu, L., Qi, L., Sun, Y., Gong, H., Chen, Y., Pei, C., et al. (2020). Mechanistic studies on peroxymonosulfate activation by g-C<sub>3</sub>N<sub>4</sub> under visible light for enhanced oxidation of light-inert dimethyl phthalate. *Chin. J. Catal.* 41, 322–332. doi:10.1016/S1872-2067(19)63447-9
- Yang, J.-C. E., Zhu, M.-P., Duan, X., Wang, S., Yuan, B., and Fu, M.-L. (2021). The mechanistic difference of 1T-2H MoS<sub>2</sub> homojunctions in persulfates activation: Structure-dependent oxidation pathways, Applied Catalysis B: *Environmental* 297, 120460. doi:10.1016/j.apcatb.2021.120460
- Yin, X., Teng, A., Zeng, Z., Meng, H., and Wu, W. (2022). Facile and novel preparation of 2D-MoS<sub>2</sub>/carbon nanodots composite with high adsorption efficiency and capacity for dye removal. *Chem. Eng. J.* 450, 138319. doi:10.1016/j.ccej.2022.138319
- Zhang, T., Huang, Z., Chen, X., Huang, M., and Ruan, J. (2016). Degradation behavior of dimethyl phthalate in an anaerobic/anoxic/oxic system. *J. Environ. Manag.* 184, 281–288. doi:10.1016/j.jenvman.2016.10.008
- Zhang, P., Gu, X., Qin, N., Hu, Y., Wang, X., and Zhang, Y. n. (2023). Y.-n. Zhang, Enhanced photoelectrocatalytic performance for degradation of dimethyl phthalate over well-designed 3D hierarchical TiO<sub>2</sub>/Ti photoelectrode coupled dual heterojunctions. *J. Hazard. Mater.* 441, 129896. doi:10.1016/j.jhazmat.2022.129896

Zhao, X., Wang, R., Zhang, J., Lu, S., Guo, Z., Hu, Z., et al. (2023). Exploring simultaneous elimination of dimethyl phthalate and nitrogen by a novel constructed wetlands coupled with dielectric barrier discharge plasma. *Chem. Eng. J.* 452, 139666. doi:10.1016/j.cej.2022.139666

Zhou, P., Zhang, J., Zhang, G., Li, W., Liu, Y., Cheng, X., et al. (2019). Degradation of dimethyl phthalate by activating peroxymonosulfate using nanoscale zero valent tungsten: Mechanism and degradation pathway. *Chem. Eng. J.* 359, 138–148. doi:10.1016/j.cej.2018.11.123

Zhou, H., Lai, L., Wan, Y., He, Y., Yao, G., and Lai, B. (2020). Molybdenum disulfide (MoS<sub>2</sub>): A versatile activator of both peroxymonosulfate and persulfate for the degradation of carbamazepine. *Chem. Eng. J.* 384, 123264. doi:10.1016/j.cej.2019.123264

Zhou, X., Xiong, W., Li, Y., Zhang, C., and Xiong, X. (2022). A novel simultaneous coupling of memory photocatalysts and microbial communities for alternate removal of dimethyl phthalate and nitrate in water under light/dark cycles. *J. Hazard. Mater.* 430, 128395. doi:10.1016/j.jhazmat.2022.128395

Zhu, L., Ji, J., Liu, J., Mine, S., Matsuoka, M., Zhang, J., et al. (2020). Designing 3D-MoS<sub>2</sub> sponge as excellent cocatalysts in advanced oxidation processes for pollutant control. *Angew. Chem. Int. Ed.* 59, 13968–13976. doi:10.1002/anie.202006059

Zhu, J., Ma, Y., Chen, X., Tang, J., Yang, L., and Zhang, Z. (2022). One-pot hydrothermal synthesis of MoS<sub>2</sub> modified sludge biochar for efficient removal of tetracycline from water. *J. Water Process Eng.* 49, 103089. doi:10.1016/j.jwpe.2022.103089